Lab on a Chip

PAPER

View Article Online
View Journal | View Issue

Cite this: *Lab Chip*, 2022, **22**, 632

Electrochemical pH regulation in droplet microfluidics†

Logan M. Wilder, Jonathan R. Thompson and Richard M. Crooks *

We report a method for electrochemical pH regulation in microdroplets generated in a microfluidic device. The key finding is that controlled quantities of reagents can be generated electrochemically in moving microdroplets confined within a microfluidic channel. Additionally, products generated at the anode and cathode can be isolated within descendant microdroplets. Specifically, ~5 nL water-in-oil microdroplets are produced at a T-junction and then later split into two descendant droplets. During splitting, floor-patterned microelectrodes drive water electrolysis within the aqueous microdroplets to produce H^+ and OH^-. This results in a change in the pHs of the descendant droplets. The droplet pH can be regulated over a range of 5.9 to 7.7 by injecting controlled amounts of charge into the droplets. When the injected charge is between −6.3 and 54.5 nC nL^{-1}, the measured pH of the resulting droplets is within ±0.1 pH units of that predicted based on the magnitude of the injected charge. This technique can likely be adapted to electrogeneration of other reagents within microdroplets.

Received 23rd October 2021,
Accepted 6th January 2022

DOI: 10.1039/d1lc00952d

rsc.li/loc

Introduction

Droplet microfluidics enables high-throughput, parallel experiments that are useful for single-entity analysis, materials synthesis, and the optimization of chemical and biochemical reactions.[1–3] However, some chemical parameters, such as pH, are difficult to externally control in droplets which are physically isolated within a continuous phase that itself is isolated within a microfluidic channel. Here, we have addressed this problem by introducing an electrochemical method for regulating the pH of moving water-in-oil microdroplets in real time. This was accomplished by driving water electrolysis in split microdroplets. The advantages of this approach are fourfold. First, droplet pH is regulated by injecting a fixed amount of charge-per-volume into each droplet. Depending on the applied potential, this results in generation of either H^+ or OH^-. Second, the products of the cathode reaction are confined within one descendant droplet while the products of the anode reaction are confined to the other descendant droplet. Separation of this nature is advantageous for generation of reagents, as demonstrated here, as well as for droplet analysis, as demonstrated by Thouin and coworkers.[4] Third, droplet pH is modified *in situ*, enabling temporal control of droplet pH. Fourth, while pH change is demonstrated here, this simple approach is generalizable to the electrochemical generation of other chemical species.

The general approach is shown in Scheme 1. Here, a microfluidic device generates ~5 nL water-in-oil droplets at a T-junction at position *i* in Scheme 1a and directs them to a splitting junction at position *ii*. Scheme 1b illustrates how the droplet is split into two descendant droplets at the perforated line of posts at position *ii*. Microelectrodes patterned on the floor of the device near the splitting junction, indicated in dark gray and labeled as "+" (anode) and "–" (cathode), drive electrochemical generation of H^+ and OH^- by water electrolysis. Because H^+ and OH^- are separated by the flow pattern of the splitting droplet, the resulting pHs of the two descendant droplets are different. As configured in Scheme 1b, H^+ is generated in the upper channel (low pH), and OH^- is generated in the lower channel (high pH).

Department of Chemistry and the Texas Materials Institute, The University of Texas at Austin, 105 E. 24th Street, Stop A5300, Austin, Texas 78712-1224, USA. E-mail: crooks@cm.utexas.edu

† Electronic supplementary information (ESI) available: Iteration 2 device geometry (Fig. S1); micrographs of pH calibrant solutions in microfluidic channels (Fig. S2); Iteration 1 device geometry (Fig. S3); a series of micrographs showing a droplet traveling through the splitting junction of an Iteration 1 device (Fig. S4); a series of micrographs showing a droplet traveling through the splitting junction of an Iteration 1 device with and without an applied voltage (Fig. S5); UV-vis absorption spectra of 10.0 μM phenol red in acidic (pH 5.8) and basic (pH 10.0) media (pathlength 1.00 cm) and UV-vis transmission spectra of the 430 nm (10 nm FWHM) and 560 nm (10 nm FWHM) bandpass filters used for the microscopy experiments (Fig. S6); discussion of calculation of measured pH in droplets; discussion of calculation of charge injected per unit volume in droplets; discussion of calculation of predicted pH as a function of charge injected per unit volume in a droplet containing phenol red; discussion of calculation of predicted pH as a function of charge delivered per unit volume in a droplet containing no buffering species. See DOI: 10.1039/d1lc00952d

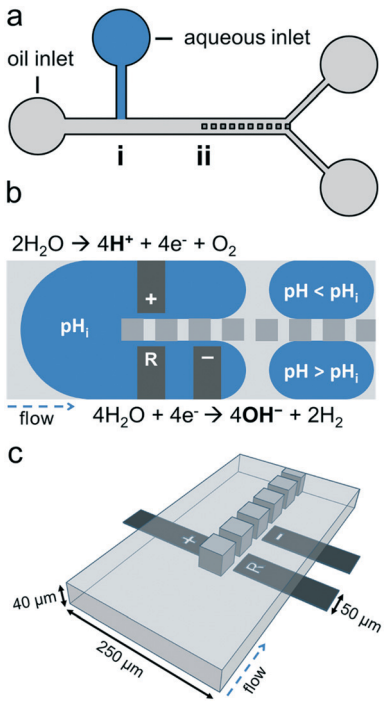

Scheme 1

Scheme 1c shows a 3D representation of the splitting junction channel geometry which is depicted as a top-down view in Scheme 1b.

Droplet microfluidics is defined by multiphase flow in which discrete volumes of one phase are separated by an immiscible continuous phase. Accordingly, each droplet represents an isolated reaction vessel which can be independently manipulated. This makes it possible to carry out parallel, high-throughput experiments in volumes in the nanoliter to femtoliter range. One common application of droplet microfluidics is analysis of single entities, including single cells,[5] single enzymes,[6] and single nucleic acids.[7] Another common application of droplet microfluidics is parameter screening of chemical and biochemical systems for optima. Such parameters include reagent concentration,[8–11] reagent identity,[12] biocatalyst identity,[13] temperature,[10,11] and reaction time.[10] Likewise, pH is another key parameter controlling chemical and biochemical reactions.

Biochemical systems in particular are sensitive to pH because protein structure and thus function is pH dependent.[14] One example is the extent of glycosylation of proteins, which can exhibit significant variation across a range of only ±0.2 pH units and represents a critical parameter in pharmaceutical biosynthesis.[15] Many abiological processes also exhibit pH dependencies, including organic synthesis,[16] nanoparticle synthesis,[17] separations,[18] and controlled release.[19–21] The combination of pH regulation and pH-mediated controlled release systems enables the regulated release of catalysts,[19] quantum dots,[19] nucleic acids,[22] and small molecules.[20,21]

Several methods for adjusting the pH of microdroplets in microfluidics have been reported. These include diffusion of acid or base from the continuous phase to the droplet phase,[23–25] activation of a photoacid within droplets,[26] and merging two droplets initially having different pHs.[27] Electrochemical pH regulation provides three benefits that are not realized in these other approaches. First, electrochemistry is inherently quantitative, and the pH in droplets can be modified by controlling the charge-per-volume delivered to each droplet. Second, electrochemistry provides excellent temporal control, because electrode voltage can be changed quickly relative to the transit time of droplets. Third, electrochemical techniques are easily integrated into microfluidics through well-established microfabrication techniques.[28]

In this paper, we describe a method for regulating the pH of ~5 nL water-in-oil droplets in a microfluidic channel. In this method, parent microdroplets are split into two descendant droplets while simultaneously passing over microelectrodes that inject charge and, hence, induce pH changes. That is, by controlling the droplet length and flow rate, controlled-current electrolysis imparts a specific amount of H^+ or OH^- into the descendant droplets. This system makes it possible to generate pH values in microdroplets ranging between 5.9 and 7.7. Importantly, when the injected charge is in the range of −6.3 to 54.5 nC nL^{-1}, the experimentally determined pHs (6.5 to 7.7) are within ±0.1 pH units of that predicted based on injected charge per droplet volume.

Experimental section

Chemicals

Polydimethylsiloxane (PDMS) was prepared using an elastomer kit (Sylgard 184, Dow Silicones Corp, Midland, MI). Tris(hydroxymethyl)aminomethane (Tris base), tris(hydroxymethyl)aminomethane hydrochloride (Tris HCl), citric acid, sodium citrate, perfluorodecalin, 1*H*,1*H*,2*H*,2*H*-perfluoro-1-octanol, 1*H*,1*H*,2*H*,2*H*-perfluorooctane-1-thiol, 1*H*,1*H*,2*H*,2*H*-perfluorooctyl-trichlorosilane, phenol red, and hexane were obtained from MilliporeSigma (Burlington, MA). Buffer solution, pH 4.00, color-coded red, buffer solution, pH 7.00, color-coded yellow, buffer solution, pH 10.00, color-coded blue, isopropanol (IPA), K_2SO_4, KNO_3, KCl, sodium phosphate (anhydrous, dibasic), sodium phosphate (monohydrate, monobasic), and glass slides were obtained from Fisher Scientific (Waltham, MA). All aqueous solutions were prepared using deionized water (DI water, >18.0 MΩ cm, Milli-Q Gradient System, MilliporeSigma).

Device fabrication

The PDMS/glass microfluidic devices were fabricated according to a previously published procedure.[29] First, a microelectrode circuit was patterned onto a glass slide using standard lift-off photo-patterning procedures.[30] The microelectrodes consisted of an adhesion layer of Ti (10 nm),

a Pt layer (100 nm) and a Ag layer (300 nm). The microelectrode positions are shown in Scheme 1b as indicated by "+" (anode), "*R*" (quasi-reference electrode), and "−" (cathode). Second, the Ag layer was removed from the anode and cathode by electrochemical oxidation (linear sweep voltammetry, LSV). The oxidation conditions were: electrolyte, 100 mM KNO_3; initial voltage = −0.20 V *vs.* Hg/$HgSO_4$/$K_2SO_{4(sat'd)}$ (MSE); final voltage = 0.33 V *vs.* MSE; and scan rate = 10 mV s^{-1}. The LSV scan was performed twice on each microelectrode. The width of the microelectrodes was 50 μm in all cases, the edge-to-edge distance between the cathode and the quasi-reference electrode was also 50 μm, and the tip-to-tip distance between the anode and the quasi-reference electrode was 60 μm.

Third, the glass slide circuit was cleaned prior to device fabrication by gentle wiping with a water-wetted paper tissue followed by sonication in IPA for 10 min. Fourth, the PDMS monolith (0.5 cm height) with inset channels (40.5 μm channel height) was fabricated using soft lithography. The geometry of the microchannels is shown in Fig. S1 of the ESI.† The main-channel width was 250 μm, the aqueous-inlet channel width was 150 μm, and the width of the outlet channels was 100 μm. The posts positioned at mid-channel in the rightmost portion of the main-channel are 40 μm by 40 μm with an edge-to-edge spacing of 20 μm. Inlet and outlet reservoirs were punched in the PDMS monolith using a 1.5 mm biopsy punch (Acuderm Inc., Ft. Lauderdale, FL), and then the PDMS monolith was cleaned by sonication in IPA for 1 min. Finally, the PDMS and glass slide were bonded by treating both with an air plasma for 45 s (plasma cleaner, "low" power setting, model PDC-32F, Harrick Scientific, Ossining, NY) followed immediately by joining. In the as-fabricated device, the microelectrodes extended ~95 μm into the channel from the channel edge.

Silanization of the microfluidic device channels

Immediately after fabrication of the microfluidic device, the channels were rendered hydrophobic by treating the interior of the channel with a 1.0% (v/v) solution of 1*H*,1*H*,2*H*,2*H*-perfluorooctyl-trichlorosilane in hexane. This was accomplished as follows. The microfluidic device channels were filled with the silane solution for 4 min, the solution was removed, and then the channels were rinsed with hexane three times. Finally, the device was heated to 100 °C for 18 h. Note that hexane swells PDMS and this was visibly apparent during the silanization procedure. The PDMS returned to its normal dimensions after the heating step. In some cases, however, the hexane-induced swelling resulted in delamination of the PDMS monolith from the glass slide. Devices damaged in this way were not used in experiments.

Operation of the microfluidic device

To form nanoliter-scale droplets in the microfluidic device, intersecting flows of aqueous and fluorocarbon oil solutions were introduced into the device inlets. Flow into the device was controlled by a syringe pump (Harvard Apparatus, Holliston, MA), and the solutions were held in 50 μL glass syringes (Hamilton Company, Reno, NV) that were connected to the microfluidic device by PTFE tubing (30.0 cm length, 1.6 mm outer diameter, 0.3 mm inner diameter (MilliporeSigma)). Unless otherwise noted, the aqueous flow rate at the inlet was 50 nL min^{-1} and the fluorocarbon oil flow rate at the inlet was 200 nL min^{-1}. The aqueous solution was composed of 10.0 mM KCl, 100 mM K_2SO_4, and 1.96 mM phenol red. The 10.0 mM KCl was added to maintain the potential stability of the Ag quasi-reference electrode. The fluorocarbon oil solution was composed of perfluorodecalin and 1*H*,1*H*,2*H*,2*H*-perfluoro-1-octanol in a ratio of 10 : 1 (v/v). 1*H*,1*H*,2*H*,2*H*-perfluorooctane-1-thiol was added to the oil phase to prevent droplet adhesion to the electrodes and the ratio of perfluorodecalin to 1*H*,1*H*,2*H*,2*H*-perfluorooctane-1-thiol was 454 : 1 (v/v). When not in use, the fluorocarbon oil solution was stored in a container purged with N_2 to avoid air saturation.

Microscopy

An inverted microscope (Nikon, Eclipse Ti2, model Ti2-D-PD, Tokyo, Japan) configured with a color camera (Nikon, DS-Fi3), a CCD camera (Andor, Ixon Life EMC, model IXON-L-897, Belfast, UK), and a white LED (Nikon, Ti2-D-LHLED) was used to image the device during operation. The microscope and cameras were operated using NIS-Elements software (Nikon, version 5.21.02). For pH imaging experiments, microfluidic devices were imaged by the CCD camera at 560 nm (5 ms exposure time) and 430 nm (20 ms exposure time) by switching between two optical bandpass filters installed on an automated rotating stage positioned in the light path between the microfluidic device and CCD camera. The white LED overhead lamp was set to 100% brightness. Switching between the bandpass filters was controlled by software and the switching time was ~0.43 s. The bandpass filters were purchased from Thorlabs Inc. (Newton, New Jersey) and had pass energies of 560 nm (10 nm FWHM) and 430 nm (10 nm FWHM). Image processing was performed with ImageJ (version 1.51j8, National Institutes of Health, USA).

Preparation and measurement of the pH calibration curve

A 16-point calibration curve was prepared using pH calibrant solutions having pHs between 5.93 and 8.55. Calibrant solutions were prepared using the following buffer solutions: pHs between 8.55 and 7.55, 100 mM Tris buffer; pHs between 7.35 and 6.18, 100 mM phosphate buffer; pH = 5.93, 100 mM citrate buffer. All calibrant solutions contained 1.96 mM phenol red. Final pHs were determined using a pH meter (Oakton Instruments, Vernon Hills, IL).

Microfluidic devices used for obtaining the calibration curve were prepared as described earlier, but with the following differences. The channel geometry was composed of five parallel channels (100 μm width, 40.7 μm height), microelectrodes were not present, and the silanization step

was omitted. The calibration curve was obtained by injecting the foregoing solutions into the channels and then imaging them three times. Micrographs of a calibration-curve device containing calibrant solutions are shown in the ESI† (Fig. S2).

Electrochemistry

All electrochemical experiments were performed using a CH Instruments Electrochemical Analyzer (Model CHI760B, Austin, TX).

Results and discussion

Droplet formation

Droplets were generated by a crossflow of immiscible fluorocarbon oil and aqueous phases at a T-junction, represented in Scheme 1a at position *i*. Unless otherwise specified, the oil phase flow rate was 200 nL min^{-1} and the aqueous phase flow rate was 50 nL min^{-1}. The average time between droplets forming at the T-junction was 5.4 ± 0.3 s (n = 10). The average droplet length, measured at the center of the droplet, was 531 ± 7 μm (n = 10), which corresponds to a droplet volume of 4.46 ± 0.06 nL.[31] Prior to reaching the splitting junction, the droplet flow rate was 420 ± 10 μm s^{-1} (n = 10). In droplet microfluidics, droplet volumes between 1–10 nL are frequently used[1] which motivated our choice to use ~5 nL droplets.

Development and description of the droplet splitting junction

Microfluidic device design is critical to both efficacious droplet splitting and electrochemical control over pH. To produce droplets having a desired pH, floor-patterned microelectrodes were used to drive water electrolysis. Water electrolysis produced enriched and spatially separated regions of H^+ and OH^- at the anode and cathode, respectively, as expressed by eqn (1) and (2).

$$2H_2O \rightarrow 4H^+ + 4e^- + O_2 \text{ (anode)} \quad (1)$$

$$4H_2O + 4e^- \rightarrow 4OH^- + 2H_2 \text{ (cathode)} \quad (2)$$

To prevent recombination of electrochemically generated H^+ and OH^-, droplets were split into descendant droplets, thereby segregating the electrolysis products. Several device designs were tested before a successful design, which enabled nearly symmetrical droplet splitting during water electrolysis, was obtained. Key insights into the splitting process emerge from consideration of this iterative process, which is described next.

An early device configuration (Iteration 1, Fig. S3†) included a T-junction for droplet formation and a T-shaped junction at which droplets were split into descendant droplets. Downstream of this junction, a porous wall connected the outlet channels. This porous wall allowed the oil phase, but not the droplets, to cross between the outlet channels. This equalizes the pressure, and thus the flow rate, between the outlet channels.[32] Equilibrating the flow rate in the outlet channels enabled symmetrical droplet splitting (Fig. S4†).

While symmetrical droplet splitting was achieved in the Iteration 1 device, the introduction of electrochemical processes complicated the experimental outcome. Specifically, when water electrolysis was driven at floor-patterned microelectrodes, the flow rate in the branch of the splitting droplet on the cathode-containing side of the splitting junction was reduced. The lower droplet flow rate over the cathode resulted in highly asymmetric splitting (or no splitting) of droplets (Fig. S5†). This is evident in the ratio of descendant droplet lengths, which was $length_{cathode\ channel}/length_{anode\ channel}$ = 0.2 ± 0.2 (n = 10). Because the width of the channels comprising the T-shaped splitting junction (30 μm) is smaller than the width of the main channel (100 μm), the flow resistance is higher in the splitting junction. This likely increased the asymmetry of the descendant droplets.

Two main changes were made between the Iteration 1 design and the final, successful iteration of the device (Iteration 2, shown in Scheme 1a and Fig. S1†). Both changes reduced flow resistance in the splitting junction, thereby improving the symmetry of droplet splitting. First, droplets were bisected by an obstacle in the center of the channel rather than by diverging channels. The obstacle consisted of a thin wall of posts (Scheme 1a, position ii). As in the Iteration 1 device, the posts act as a porous wall, which equilibrates pressure between the outlet channels.[32] Second, the channel height was increased by a factor of ~2.2 with respect to the Iteration 1 geometry. These two changes to the device design enabled nearly symmetrical splitting of droplets during water electrolysis. This is evident in the much improved ratio of descendant droplet lengths at the highest current magnitude used in this study (80 nA): $length_{cathode\ channel}/length_{anode\ channel}$ = 0.81 ± 0.01, n = 10. At lower applied currents, the droplet splitting ratio is further improved. For instance, this ratio at the lowest applied current (10 nA) was $length_{cathode\ channel}/length_{anode\ channel}$ = 0.932 ± 0.008, n = 10. When the microelectrodes were inactive, droplets split symmetrically in Iteration 2 geometry channels.

In addition to the challenges associated with attaining symmetrical droplet splitting, we also found that droplets would often adhere to one of the microelectrodes. These droplets obstructed flow, resulting in asymmetrical droplet splitting. We found there were two specific types of droplet-electrode adhesion. First, droplets would sometimes adhere to electrodes before a voltage was applied. This occurred in about 25% of the devices. Second, in some cases, droplets would not adhere before applying a voltage to the electrodes, but as soon as a voltage sufficient to drive water electrolysis was applied, droplets would adhere to either the cathode or the anode. It is unlikely that this observation was due to reversible electrowetting,[33] because the droplet remained adherent for at least 5 min after the voltage was turned off.

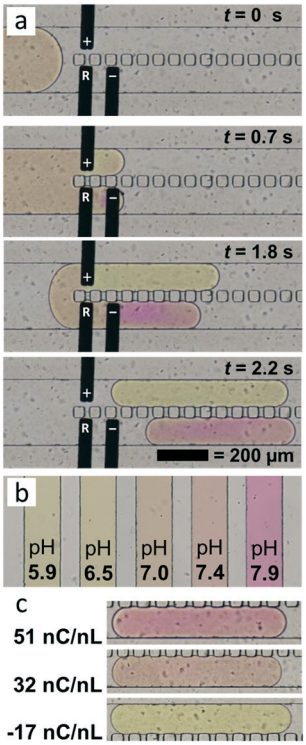

Fig. 1 (a) Series of micrographs showing splitting of an aqueous microdroplet into a pair of descendant droplets while water electrolysis is driven at the anode (+) and cathode (–) microelectrodes. (b) Micrographs of static buffered aqueous solutions containing phenol red at the indicated pHs. The colors in the micrographs can be compared to those of split microdroplets to estimate their pH. (c) Micrographs of descendant microdroplets after injection of the indicated amounts of charge. The different colors represent pH changes driven by water electrolysis.

To overcome the problem of droplet adherence, a fluorinated alkylthiol, 1*H*,1*H*,2*H*,2*H*-perfluorooctane-1-thiol, was added to the oil phase. During the experiment, the thiol in the oil phase likely forms a partial hydrophobic monolayer on the microelectrodes, thereby eliminating droplet adhesion for current magnitudes ≤ 80 nA (at higher currents, droplets would sometimes still adhere to the anode). Because it is unlikely that the thiol forms a complete monolayer, it does not significantly interfere with water electrolysis. Finally, it is important to note that at flow rates lower than that which we report (*e.g.*, 100 nL min^{-1} oil, 50 nL min^{-1} aqueous), droplet adhesion to the electrodes occurred even with 1*H*,1*H*,2*H*,2*H*-perfluorooctane-1-thiol present in the oil phase.

Regulation of the pH in microdroplets

Electrochemical methods have previously been applied to the analysis[4,34–43] and manipulation[44–46] of microdroplet contents. In an early example, Zheng and coworkers[41] used electrochemistry to carry out chronoamperometry. In this case, the droplets encountered two microwire electrodes within a microfluidic channel that completed an electrical circuit. Building on this work, our group[37] demonstrated that chronoamperometric analysis of microdroplets could be carried out using floor-patterned microelectrodes, thereby avoiding the need for integration of microwire electrodes into devices. The present work takes our earlier study a step further by intentionally electrogenerating (not just analyzing) precise amounts of reagents within moving microdroplets.[47]

The mechanism of droplet pH change is illustrated in Scheme 1b. Here, a water-in-oil droplet splits into descendant droplets while floor-patterned microelectrodes simultaneously drive water electrolysis in the branches of the splitting droplet. After the droplet is fully split, the acidic and basic regions are permanently isolated within the descendant droplets.

Fig. 1a is a series of micrographs showing a droplet moving through the splitting junction of the microchannel. At t = 0 s, the potentiostat is set to apply 80 nA to the electrodes, but the fluorocarbon oil phase blocks current flow between the microelectrodes. At t = 0.7 s, a droplet enters the splitting junction and completes the circuit between the microelectrodes. At this point, water electrolysis begins to produce H^+ and OH^- at the anode and cathode, respectively (eqn (1) and (2)). Water electrolysis proceeds as long as the microdroplet completes the circuit. The resulting pH change is apparent from the pH indicator color changes at t = 1.8 s. Upon leaving the splitting junction at t = 2.2 s, droplet splitting is complete and the water electrolysis products (H^+ and OH^-) are segregated in the descendant droplets. For comparison with the colors in Fig. 1a, Fig. 1b shows buffered phenol red calibrant solutions over the pH range of 5.9–7.9.

The foregoing results are significant for two reasons. First, and most generally, it demonstrates that electrogenerated products formed at the anode and cathode can be isolated *via* microdroplet splitting. Second, the colors of the descendant droplets indicate that it is possible to, at least qualitatively, control the pH within microdroplets.

To determine the range over which pH within microdroplets can be controlled, we repeated the foregoing experiment but with different magnitudes of current passing

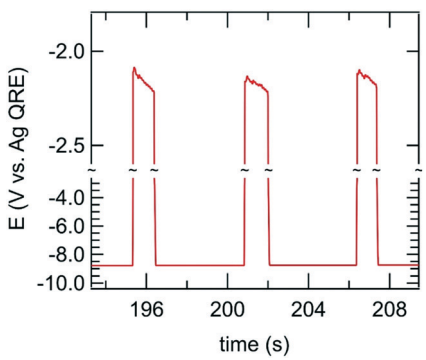

Fig. 2 Chronopotentiogram (80 nA constant-current) showing the potential of the cathode during the passage of three droplets through the splitting junction of the microfluidic device. The vertical axis represents the potential of the cathode microelectrode *vs.* Ag quasi-reference electrode (Ag QRE). The droplet solution contained 10.0 mM KCl to stabilize the potential of the Ag QRE.

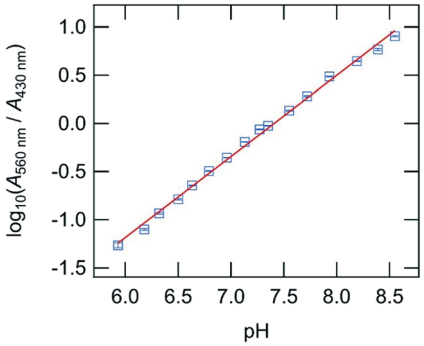

Fig. 3 Ratiometric colorimetry calibration curve for the determination of droplet pH. Each point represents the average value and standard deviation of three measurements. Error bars are present in the figure but in all cases are shorter than the height of the blue boxes. Linear regression of the calibration curve is represented by the red line. The vertical axis represents the logarithm of the ratio of absorption at 560 nm *vs.* 430 nm (corresponding to the deprotonated and protonated forms of phenol red, respectively). The concentration of phenol red was 1.96 mM. The absorption at each wavelength is the logarithm of the ratio of the intensity of light (I_0) passing through the PDMS monolith, but not through the microfluidic channel, to the intensity of light (I) passing through the microfluidic device at the position of the microfluidic channel containing calibrant solution such as the solutions shown in Fig. 1b. The horizontal axis represents the pH of the calibrant solutions measured using an electrochemical pH meter. The slope of the linear regression line was 0.84 and R^2 = 0.997.

through the microelectrodes. Fig. 1c shows selected results from experiments in which the total charge injected into droplets passing over the cathode or anode ranged from −17.9 to 54.5 nC nL^{-1}. Comparison to the calibration standards in Fig. 1b indicates a pH range of 5.9 to 7.7. Additional discussion relating to pH range and quantification will be presented later.

Fig. 2 is a representative chronopotentiogram obtained at 80 nA. It shows how the potential of the cathode, measured *vs.* the Ag quasi-reference electrode (Ag QRE), changes as a function of time during the passage of three droplets. The position of the Ag QRE is shown in Scheme 1 and Fig. 1a. The chronopotentiogram provides non-optical and time-resolved information about droplet frequency and residence time.

The potential of the cathode between the voltage excursions (*e.g.*, 198–200 s) represents the time during which oil flows over the electrodes. During this time the circuit is incomplete, and therefore the potential is close to the compliance voltage of the potentiostat (±10 V). The three low-magnitude potential regions, which have left edges at 195.3, 200.8, and 206.3 s, indicate times when the electrochemical circuit is complete and droplets are moving over the electrodes. During the droplet residence time, the potential of the cathode quickly shifts to the voltage required to drive a constant current of 80 nA.

During droplet pH adjustment, H_2 and O_2 gases are formed as shown by eqn (1) and (2). Gas bubbles did not appear at the anode, but in some cases, small gas bubbles formed at the cathode. For example, in a test of three replicate devices at 80 nA applied current, the percentage of droplet splitting events which were accompanied by bubble formation differed from device to device and ranged between 15–64%. In all cases, these bubbles did not exceed 10 μm in diameter and dissipated within 2 s of formation. Bubble formation did not appear to affect device performance. Perfluorodecalin is characterized by a large capacity to dissolve both H_2 and O_2, which likely assisted in the dissipation of electrogenerated bubbles.

Measurement of pH in microdroplets by ratiometric colorimetry

Measurement of pH in microchannels has previously been carried out using fluorimetry,[25,48,49] colorimetry,[50–52] and electrochemical methods.[40,53–55] We used ratiometric colorimetry to quantitatively measure microdroplet pH.[52] Ratiometric colorimetry is a robust method for microfluidic pH measurement as it is insensitive to variation in pathlength and dye concentration.

A discussion of the theoretical basis for microdroplet pH measurement by ratiometric colorimetry is provided in the ESI.† Briefly, the concentration ratio of the deprotonated-to-protonated forms of a weak acid is related to solution pH by the Henderson–Hasselbalch equation. Phenol red exhibits absorbance maxima at 560 nm when deprotonated and 430 nm when protonated (UV-vis spectra shown in Fig. S6 of the ESI†).[52] By sequentially measuring the absorbance of droplets at these wavelengths, the ratio of deprotonated-to-protonated forms of phenol red can be obtained. This ratio can then be used to calculate droplet pH using a calibration curve. Fig. 3 shows the calibration curve relating the logarithm of the measured absorbance ratio of deprotonated-to-protonated phenol red to droplet pH. The calibration curve exhibits a linear response in the pH range 5.9 to 8.6.

Quantifying electrochemically-induced pH changes in microdroplets

The results of microdroplet pH regulation experiments are shown in Fig. 4. Each blue square represents the measured pH of a single droplet. The black line is the pH predicted on

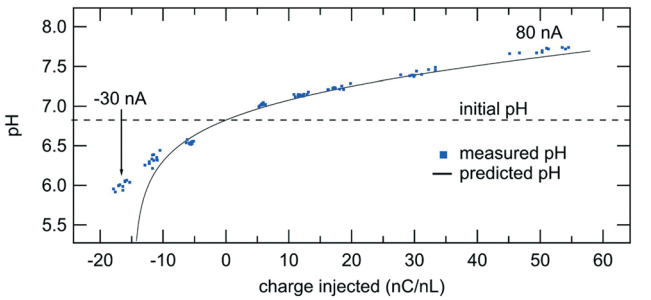

Fig. 4 Measured and predicted pH of descendant microdroplets after water electrolysis as a function of injected charge-per-volume. The initial pH of the droplets was 6.8. Some blue squares overlap due to close grouping and thus appear as larger blue squares.

the basis of the measured amount of charge injected into droplets. A discussion of the calculation of charge injected per unit volume, as well as the calculation of predicted pH, is included in the ESI.† Briefly, the charge was calculated from the applied current, the cross-sectional area of the droplets, and the individually measured flow rate of the descendant droplets traveling past the anode or cathode microelectrodes. An assumption in this calculation is that the current efficiency for water electrolysis is 100%. The predicted pH was calculated on the basis of the buffering capacity of 1.96 mM phenol red (pK_a = 7.9) using the Henderson–Hasselbalch equation. The initial pH of the microdroplets (pH = 6.8) was measured before they encountered the microelectrodes at a channel position 200 μm upflow of the splitting junction.

Fig. 4 shows that there are eight spatially distinct groups of droplet pH measurements, each representing a different applied current: −30 nA, −20 nA, −10 nA, 10 nA, 20 nA, 30 nA, 50 nA and 80 nA from left to right. Droplet pHs resulting from currents below −30 nA were outside of the linear range of the calibration curve. The droplet pH regulation experiment was tested and found to reproducibly produce split droplets having the desired pH for at least 5 min (~55 microdroplets) at each applied current. The run time for replicates of the general experiment at different applied currents was arbitrarily chosen to be 5 min. In each replicate, droplet flow remained stable when the experiment was terminated.

The data shown in Fig. 4 indicate that the predicted and measured pH agree to within ±0.1 pH units when the injected charge is in the range of −6.3 to 54.5 nC nL^{-1}. This range of charges corresponds to pH values between 6.5 and 7.7. For injected charge values more negative than −6.3 nC nL^{-1}, the agreement between the experimental and predicted pH is poorer than for higher charges. This deviation likely arises from the presence of dissolved CO_2 in the droplets. Specifically, under the conditions used for our experiments, some dissolved CO_2 is present and in equilibrium with H_2CO_3 (apparent pK_a = 6.36),[56] which contributes to the buffering capacity of the system. Because dissolved CO_2 is not accounted for in the predicted pH model, the experimental pH changes are less extreme than the predicted values.

Finally, it is important to note that the experimentally observed pH changes are limited by the buffering capacity of the phenol red indicator dye. If no buffering species were present in the droplets and pH depended only on electrochemically generated H^+ or OH^-, a pH range between 4.0 and 10.0 should be achievable with the application of only ±10.0 nC nL^{-1} (discussion of calculation provided in the ESI†). However, as pH-responsive systems will necessarily exhibit some capacity to react with H^+ or OH^-, the demonstration here of pH change in droplets containing a dilute buffer represents a realistic model system. While only a single droplet solution composition was tested here (100 mM K_2SO_4, 10.0 mM KCl, 1.96 mM phenol red), this technique should be amenable to other solution compositions. For pH adjustment experiments, the buffering capacity of the solution should be considered. Additionally, the presence of solution components which reduce or oxidize at the same applied potential as the target analyte should be considered. Finally, note that the presence of an electrolyte is necessary.

Summary and conclusions

We have reported a method for pH regulation of water-in-oil microdroplets moving within a microfluidic channel. The key finding is that predictable quantities of reagents can be electrogenerated in droplets using floor-patterned microelectrodes, and, further, that the products from the anode and cathode can be isolated within separate droplets. We demonstrated this by splitting droplets while simultaneously applying a current to generate H^+ or OH^- in the descendant droplets. This results in descendant droplets having pHs that align with those predicted based on the charge injected associated with water electrolysis. Importantly, electrochemically-induced pH changes occur *in situ*, and this enables temporal pH control within droplets.

In addition to demonstrating control over microdroplet pH, we also developed a general device design for splitting microdroplets into nearly identical pairs of descendant droplets while microelectrodes drive electrolysis in the branches of the splitting droplet. We further showed that application of an electrochemical potential to the electrodes introduces problems related to droplet-electrode adherence. This problem was resolved by introducing a dynamic partial surfactant monolayer to the electrode surface.

We conclude that the approach shown here is generally applicable to droplet splitting during microelectrochemical processes. Accordingly, this methodology will likely find application in other chemical and biochemical systems that benefit from pH control. Electrochemical processes other than water electrolysis are also amenable to the device design.

Conflicts of interest

There are no conflicts to declare.

Acknowledgements

We gratefully acknowledge support from the Chemical Sciences, Geosciences, and Biosciences Division, Office of Basic Energy Sciences, Office of Science, U.S. Department of Energy (Grant: DE-FG02-06ER15758). We thank the Robert A. Welch Foundation (Grant F-0032) for sustained support of our research program. Microscopy imaging was performed at the Center for Biomedical Research Support Microscopy and Imaging Facility at UT Austin (RRID# SCR_021756). We would also like to thank the following individuals for helpful suggestions with various aspects of the results provided herein: Dr. Peixin He (CH Instruments, Austin, TX), Dr. Collin D. Davies (Plummer Associates, Inc, Austin, TX), and Prof.

Robert T. Kennedy and Mr. Emory M. Payne (University of Michigan, Ann Arbor, MI).

References

1 Y. Ding, P. D. Howes and A. J. deMello, *Anal. Chem.*, 2020, **92**, 132–149.
2 L. Shang, Y. Cheng and Y. Zhao, *Chem. Rev.*, 2017, **117**, 7964–8040.
3 T. S. Kaminski and P. Garstecki, *Chem. Soc. Rev.*, 2017, **46**, 6210–6226.
4 T. Abadie, C. Souprayen, C. Sella and L. Thouin, *Electrochim. Acta*, 2021, **393**, 139017.
5 Z. Yu, L. Zhou, T. Zhang, R. Shen, C. Li, X. Fang, G. Griffiths and J. Liu, *ACS Sens.*, 2017, **2**, 626–634.
6 R. Arayanarakool, L. Shui, S. W. M. Kengen, A. van den Berg and J. C. T. Eijkel, *Lab Chip*, 2013, **13**, 1955–1962.
7 Y. Schaerli, R. C. Wootton, T. Robinson, V. Stein, C. Dunsby, M. A. A. Neil, P. M. W. French, A. J. deMello, C. Abell and F. Hollfelder, *Anal. Chem.*, 2009, **81**, 302–306.
8 I. Lignos, V. Morad, Y. Shynkarenko, C. Bernasconi, R. M. Maceiczyk, L. Protesescu, F. Bertolotti, S. Kumar, S. T. Ochsenbein, N. Masciocchi, A. Guagliardi, C.-J. Shih, M. I. Bodnarchuk, A. J. deMello and M. V. Kovalenko, *ACS Nano*, 2018, **12**, 5504–5517.
9 L. Bezinge, R. M. Maceiczyk, I. Lignos, M. V. Kovalenko and A. J. deMello, *ACS Appl. Mater. Interfaces*, 2018, **10**, 18869–18878.
10 I. Lignos, S. Stavrakis, G. Nedelcu, L. Protesescu, A. J. deMello and M. V. Kovalenko, *Nano Lett.*, 2016, **16**, 1869–1877.
11 I. Lignos, L. Protesescu, D. B. Emiroglu, R. Maceiczyk, S. Schneider, M. V. Kovalenko and A. J. deMello, *Nano Lett.*, 2018, **18**, 1246–1252.
12 A. B. MacConnell, A. K. Price and B. M. Paegel, *ACS Comb. Sci.*, 2017, **19**, 181–192.
13 D. Vallejo, A. Nikoomanzar, B. M. Paegel and J. C. Chaput, *ACS Synth. Biol.*, 2019, **8**, 1430–1440.
14 J. Antosiewicz, J. A. McCammon and M. K. Gilson, *J. Mol. Biol.*, 1994, **238**, 415–436.
15 J. Müthing, S. E. Kemminer, H. S. Conradt, D. Šagi, M. Nimtz, U. Kärst and J. Peter-Katalinić, *Biotechnol. Bioeng.*, 2003, **83**, 321–334.
16 M. A. Martínez-Aguirre, R. Villamil-Ramos, J. A. Guerrero-Alvarez and A. K. Yatsimirsky, *J. Org. Chem.*, 2013, **78**, 4674–4684.
17 Y. Qin, X. Ji, J. Jing, H. Liu, H. Wu and W. Yang, *Colloids Surf., A*, 2010, **372**, 172–176.
18 J.-M. Sun, F. Li and J.-C. Huang, *Ind. Eng. Chem. Res.*, 2006, **45**, 1557–1562.
19 F. Huang, W.-C. Liao, Y. S. Sohn, R. Nechushtai, C.-H. Lu and I. Willner, *J. Am. Chem. Soc.*, 2016, **138**, 8936–8945.
20 Z. Xu, S. Liu, Y. Kang and M. Wang, *Nanoscale*, 2015, **7**, 5859–5868.
21 N. M. Khashab, M. E. Belowich, A. Trabolsi, D. C. Friedman, C. Valente, Y. Lau, H. A. Khatib, J. I. Zink and J. F. Stoddart, *Chem. Commun.*, 2009, 5371–5373.
22 E. Fattal, P. Couvreur and C. Dubernet, *Adv. Drug Delivery Rev.*, 2004, **56**, 931–946.
23 P. Abbyad, R. Dangla, A. Alexandrou and C. N. Baroud, *Lab Chip*, 2011, **11**, 813–821.
24 S. Mashaghi and A. M. van Oijen, *Sci. Rep.*, 2015, **5**, 11837.
25 M. Tovar, L. Mahler, S. Buchheim, M. Roth and M. A. Rosenbaum, *Microb. Cell Fact.*, 2020, **19**, 16.
26 M. Marquis, V. Alix, I. Capron, S. Cuenot and A. Zykwinska, *ACS Biomater. Sci. Eng.*, 2016, **2**, 535–543.
27 D. Tanaka, S. Sawai, S. Hattori, Y. Nozaki, D. H. Yoon, H. Fujita, T. Sekiguchi, T. Akitsu and S. Shoji, *RSC Adv.*, 2020, **10**, 38900–38905.
28 D. G. Rackus, M. H. Shamsi and A. R. Wheeler, *Chem. Soc. Rev.*, 2015, **44**, 5320–5340.
29 J. C. McDonald, D. C. Duffy, J. R. Anderson, D. T. Chiu, H. Wu, O. J. A. Schueller and G. M. Whitesides, *Electrophoresis*, 2000, **21**, 27–40.
30 J. R. Thompson, L. M. Wilder and R. M. Crooks, *Chem. Sci.*, 2021, **12**, 13744–13755.
31 M. Musterd, V. van Steijn, C. R. Kleijn and M. T. Kreutzer, *RSC Adv.*, 2015, **5**, 16042–16049.
32 J. Nie and R. T. Kennedy, *Anal. Chem.*, 2010, **82**, 7852–7856.
33 W. C. Nelson and C.-J. Kim, *J. Adhes. Sci. Technol.*, 2012, **26**, 1747–1771.
34 H. Goto, Y. Kanai, A. Yotsui, S. Shimokihara, S. Shitara, R. Oyobiki, K. Fujiwara, T. Watanabe, Y. Einaga, Y. Matsumoto, N. Miki and N. Doi, *Lab Chip*, 2020, **20**, 852–861.
35 Z. Han, Y. Y. Chang, S. W. N. Au and B. Zheng, *Chem. Commun.*, 2012, **48**, 1601–1603.
36 A. Leroy, J. Teixidor, A. Bertsch and P. Renaud, *Lab Chip*, 2021, **21**, 3328–3337.
37 H. Liu and R. M. Crooks, *Lab Chip*, 2013, **13**, 1364–1370.
38 X. Hu, X. Lin, Q. He and H. Chen, *J. Electroanal. Chem.*, 2014, **726**, 7–14.
39 P. Rattanarat, A. Suea-Ngam, N. Ruecha, W. Siangproh, C. S. Henry, M. Srisa-Art and O. Chailapakul, *Anal. Chim. Acta*, 2016, **925**, 51–60.
40 J. Schütt, B. Ibarlucea, R. Illing, F. Zörgiebel, S. Pregl, D. Nozaki, W. M. Weber, T. Mikolajick, L. Baraban and G. Cuniberti, *Nano Lett.*, 2016, **16**, 4991–5000.
41 Z. Han, W. Li, Y. Huang and B. Zheng, *Anal. Chem.*, 2009, **81**, 5840–5845.
42 T. Abadie, C. Sella and L. Thouin, *Electrochem. Commun.*, 2017, **80**, 55–59.
43 T. Delahaye, T. Lombardo, C. Sella and L. Thouin, *Anal. Chim. Acta*, 2021, **1155**, 338344.
44 H. Zhou and S. Yao, *Lab Chip*, 2013, **13**, 962–969.
45 S. Kim, B. Ganapathysubramanian and R. K. Anand, *J. Am. Chem. Soc.*, 2020, **142**, 3196–3204.
46 H. Zhou, G. Li and S. Yao, *Lab Chip*, 2014, **14**, 1917–1922.
47 H. Dau, C. Limberg, T. Reier, M. Risch, S. Roggan and P. Strasser, *ChemCatChem*, 2010, **2**, 724–761.
48 N. M. Contento, S. P. Branagan and P. W. Bohn, *Lab Chip*, 2011, **11**, 3634–3641.

49 M. P. Gashti, J. Asselin, J. Barbeau, D. Boudreau and J. Greener, *Lab Chip*, 2016, **16**, 1412–1419.
50 X. Xu, S. Smith, J. Urban and Z. Cui, *Med. Eng. Phys.*, 2006, **28**, 468–474.
51 K. Macounová, C. R. Cabrera, M. R. Holl and P. Yager, *Anal. Chem.*, 2000, **72**, 3745–3751.
52 E. B. Magnusson, S. Halldorsson, R. M. T. Fleming and K. Leosson, *Biomed. Opt. Express*, 2013, **4**, 1749–1758.
53 I. A. Ges, B. L. Ivanov, D. K. Schaffer, E. A. Lima, A. A. Werdich and F. J. Baudenbacher, *Biosens. Bioelectron.*, 2005, **21**, 248–256.
54 A. Yamada and M. Suzuki, *Sensors*, 2017, **17**, 1563.
55 Y.-T. Tsai, S.-J. Chang, L.-W. Ji, Y.-J. Hsiao and I.-T. Tang, *ACS Omega*, 2019, **4**, 19847–19855.
56 X.-X. Wang, H. Fu, D.-M. Du, Z.-Y. Zhou, A.-G. Zhang, C.-F. Su and K.-S. Ma, *Chem. Phys. Lett.*, 2008, **460**, 339–342.